



Application of physical electric circuit modeling to characterize Li-ion battery electrochemical processes



M. Greenleaf, H. Li, J.P. Zheng*

^a Department of Electrical and Computer Engineering, Florida A&M University and Florida State University, Tallahassee, FL 32312, USA

^b Aero-Propulsion, Mechatronics and Energy Center, Florida State University, Tallahassee, FL 32312, USA

^c Center for Advanced Power Systems, Florida State University, Tallahassee, FL 32312, USA

HIGHLIGHTS

- A physical electric circuit model was used to model two similar Li-ion batteries with different cathodes.
- The use of this model allowed calculation of exchange current density, diffusion coefficient, and double layer capacitance.
- This approach allowed us to determine the corresponding electrode that represented these behaviors.
- This approach was non-destructive to full-cell batteries.

ARTICLE INFO

Article history:

Received 20 March 2014

Received in revised form

20 June 2014

Accepted 14 July 2014

Available online 21 July 2014

Keywords:

Li-ion battery

Electric circuit model

Electrochemical impedance spectroscopy

Li_xFePO_4

Li_xCoO_2

ABSTRACT

A physical electric circuit model (PECM) was used to identify several electrochemical processes occurring in two commercial Li-ion batteries of different cathode materials (Li_xFePO_4 and Li_xCoO_2) via electrochemical impedance spectroscopy (EIS). Through defining these electrochemical processes in these two cells, it was determined that the charge transfer resistance (or exchange current density) observed via EIS was due to the cathodic exchange current densities in both the Li_xFePO_4 and Li_xCoO_2 full cells. In discussing the ionic diffusion of the examined cells, the anode of one cell and the cathode of the other were primarily responsible for the observed diffusion of the full cells. Lastly, the measured double layer capacitance was determined to be represented in EIS scans by the anodes of both full cells. The diffusion coefficient was calculated using Fick's 1st Law estimation, and from this coefficient, the particle size was calculated and evaluated against scanning electron microscopy (SEM).

© 2014 Elsevier B.V. All rights reserved.

1. Introduction

Lithium-ion batteries (Li-ion batteries or LIBs) have been commercially available for more than 20 years. From work begun by Goodenough et al. and Sony Corporation [1,2], many cathode and anode materials have been investigated for use in their construction. In current production, two cathode chemistries, namely Li_xFePO_4 and Li_xCoO_2 , have grown in popularity while hard carbon (HC) and graphite have been used primarily as anodes. These materials are well researched with their materials well documented.

To date, extensive work has been carried out in determining the physical parameters and performance of battery materials in a

variety of ways. Zhou et al. [3] have used electrochemical impedance spectroscopy (EIS) and X-ray diffraction (XRD) to provide insight into nanoporous cathode mechanisms including phase transitions of cathode materials during charge and discharge. Osiak et al. [4] reported on the structural and electrochemical characteristics of SnO_2 , In_2O_3 , and Sn doped In_2O_3 nanoparticles used as a battery anode using scanning electron microscopy (SEM) and energy-dispersive X-ray spectroscopy (EDX) techniques. Levi and Aurbach [5] and Della'Era and Pasquali [6] have also used intermittent titration techniques (PITT) and EIS to measure the diffusion coefficient of battery materials, and have shown that EIS- and PITT-measured diffusion coefficients are similar.

Electrochemical impedance spectroscopy (EIS) is a mature and useful tool in characterizing electrochemical systems. To increase usefulness, equivalent circuit modeling has been employed to provide physical or phenomenological representations of observed electrochemical behavior. Examples of the usefulness of this

* Corresponding author. Department of Electrical and Computer Engineering, Florida A&M University and Florida State University, Tallahassee, FL 32312, USA.
E-mail address: zheng@eng.fsu.edu (J.P. Zheng).

technique can be found many places in literature: Mauracher and Karden [7,8] were able to apply this modeling to lead-acid batteries to determine important battery parameters with a high degree of accuracy. Stephen Buller [9] also applied this method for automotive applications. Moss et al. were able to use this method to determine various features of energy storage devices including electrochemical capacitors [10] and Li-polymer batteries [11–13].

In this paper, a physical electric circuit model (PECM) discussed previously [14] was applied to EIS data gathered on two commercial Li-ion batteries of similar dimension and structure (except for cathode material) to determine if it is possible to define and quantify the electrochemical processes inside a Li-ion battery using only EIS and other in-situ processes. The term PECM is used here to define an electric circuit derived from a physics-based phenomenological model, not simply an electrical analog circuit [15]. This work shows the significance of PECM as a preferential method to analyzing battery performance and highlights the ability of PECM and EIS to determine the factors affecting cell performance.

2. Experimental

Both cells used in this experiment are commercially available RCR123A cells from Powerizer® with details listed in Table 1. The Li_xFePO_4 -cathode cell and the Li_xCoO_2 -cathode cell were assigned the names of LFP and LCO respectively. As was done previously [14], both cells were subjected to potentiostatic EIS measurements using a Solartron™ 1280B Frequency Response Analyzer at uniform states of charge (every 10% SOC). The frequency range for this test ranged from 20 kHz to 10 mHz with 0 V DC offset and an AC magnitude of 10 mV.

3. Modeling

Select resulting spectra for both cells are presented in Fig. 1. From previous work [14] the EIS data was fit in the frequency domain using electric circuit elements as shown in Fig. 2. While Ciucci et al. have developed a novel EIS parameter evaluation methodology [16,17], each element was fit in Scribner and Associates' Zplot® software using a Calc-modulus data weighing, complex fitting, iterative method. The returned accuracy of each element per EIS scan was below 20%. Also it should be noted that successive EIS

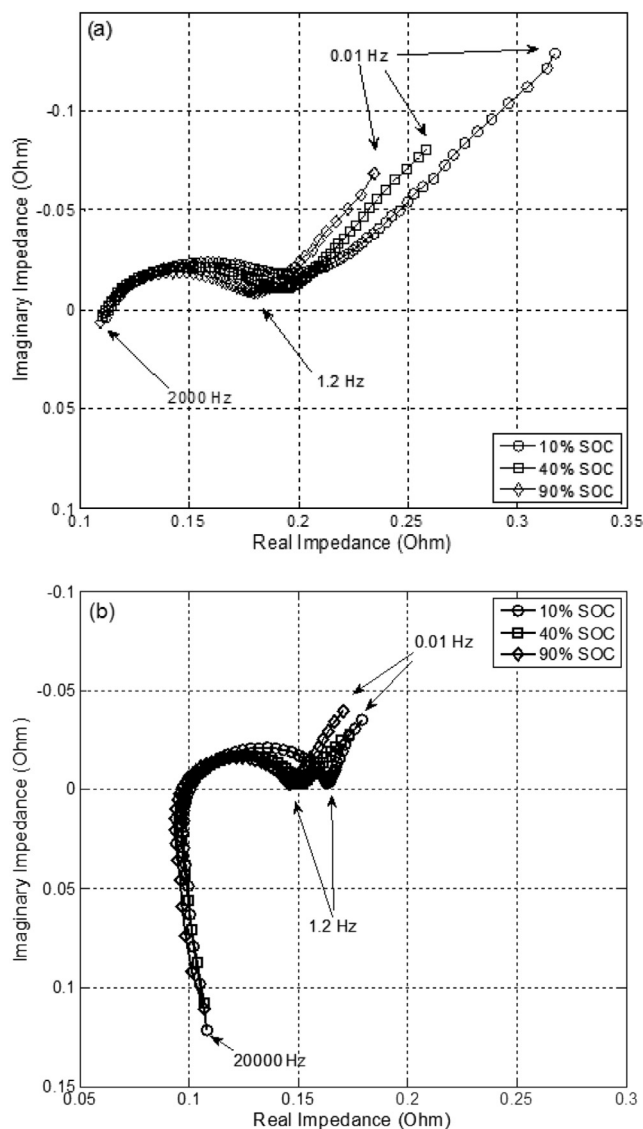


Fig. 1. EIS result at various SOC for (a) LFP and (b) LCO cells.

Table 1
Measurement of battery electrodes.

Parameter	LFP	LCO	Unit
Capacity	450	650	mAh
Electrode anode length	581.34	499.14	mm
Electrode anode width	25.12	26.06	mm
Electrode anode thickness	0.12	0.17	mm
Electrode cathode length	547.83	482.83	mm
Electrode cathode width	24.15	24.79	mm
Electrode cathode thickness	0.14	0.14	mm
Separator length	982.35	977.52	mm
Separator width	26.3	26.309	mm
Separator thickness	0.02	0.02	mm
Cu current collector thickness	0.01	0.01	mm
Al current collector thickness	0.01	0.01	mm
Anode half cell weight	3.6295	4.2275	g
Cathode half cell weight	5.1594	5.7876	g
Anode weight	2.324	2.9904	g
Cathode weight	4.8022	5.4661	g
Cu volume	0.146	0.1383	cm ³
Al volume	0.1323	0.119	cm ³
Cu weight	1.3055	1.2371	g
Al weight	0.3572	0.3214	g
Anode electrode area	292.06	260.15	cm ²
Cathode electrode area	264.6	239.38	cm ²

scans of the same cell at the same SOC yielded a nearly identical impedance spectra (hence the lack of error bars in Fig. 1).

By assigning certain circuit elements to electrochemical processes, we may evaluate the EIS spectra of each battery and determine (for the full cell) the processes that affect cell performance. These elements and their corresponding processes are defined as follows:

L describes the inductance observed in the Nyquist plots which correspond to the inductance of the experimental leads and of the spiral wound nature of the cells. R_s describes the equivalent ohmic series resistance of separator, solution and contact resistances [18,19] in the cells. Elements R_1 through R_3 and C_1 through C_3 describe the formation of solid electrolyte interface (SEI) which form on the surface of the anode [7,20,21] during initial cycling and which grow through successive cycling. Three RC circuits were chosen in this model to fit the SEI layer due to the semi-elliptical nature of the SEI region which could be modeled by several RC circuits with overlapping spectra. R_{ct} refers to the charge transfer resistance, a non-ohmic reaction resistance that relates the activation overpotential and exchange current density as described by the Butler–Volmer equation for the transfer of charge carriers

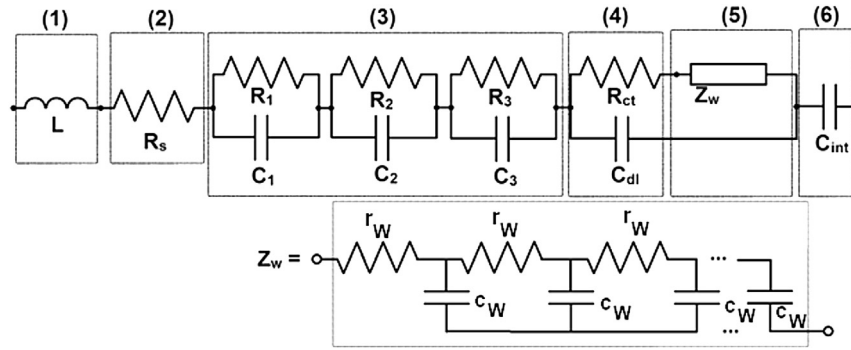


Fig. 2. Physical equivalent circuit model used to describe EIS data. Note: R_W is the summation of r_W and C_W is the summation of c_W . For this circuit (1) represents the line and spiral wound inductance of the cell, (2) represents the resistance of the solution and separator, (3) represents the SEI layer, (4) represents charge transfer kinetics, (5) represents ionic diffusion into cathode and anode matrices, and (6) represents the intercalation capacitance of Li-ions in the host matrices.

through the solid/electrolyte boundary and C_{dl} describes the accumulation of charge carriers at the previously stated boundary condition and the resulting double-layer capacitance that forms as modeled by Guoy-Chapman [20,22]. The variables T_W , R_W , and p refer to the diffusion time, Warburg resistance, and ideality factor (respectively) used to define the Warburg equation (Z_W) for semi-infinite diffusion which describes the semi-infinite diffusion of charge carriers through media [14,15,22–24]. Lastly C_{int} defines the intercalation capacitance of the host materials.

To suitably model these parameters, equations fitting each parameter as a function of SOC were developed. Fig. 3 depicts these equations as they fit parameter as a function of SOC. Based upon these equations, and through the application of Ohm's law and Inverse Fourier Transform, we can determine the terminal voltage

of the battery as depicted in Fig. 4 which is governed by the following equations:

$$V_T(\text{SOC}) = U(\text{SOC}) - \left[V_{R_s}(\text{SOC}) + V_{SEI}(\text{SOC}) + V_{ct||dl}(\text{SOC}) + V_{cint}(\text{SOC}) + V_{Warburg}(\text{SOC}) \right] \quad (1)$$

where U is the open circuit voltage of the cell at a given SOC,

$$V_{R_s}(\text{SOC}) = I \times R_s(\text{SOC}) \quad (2)$$

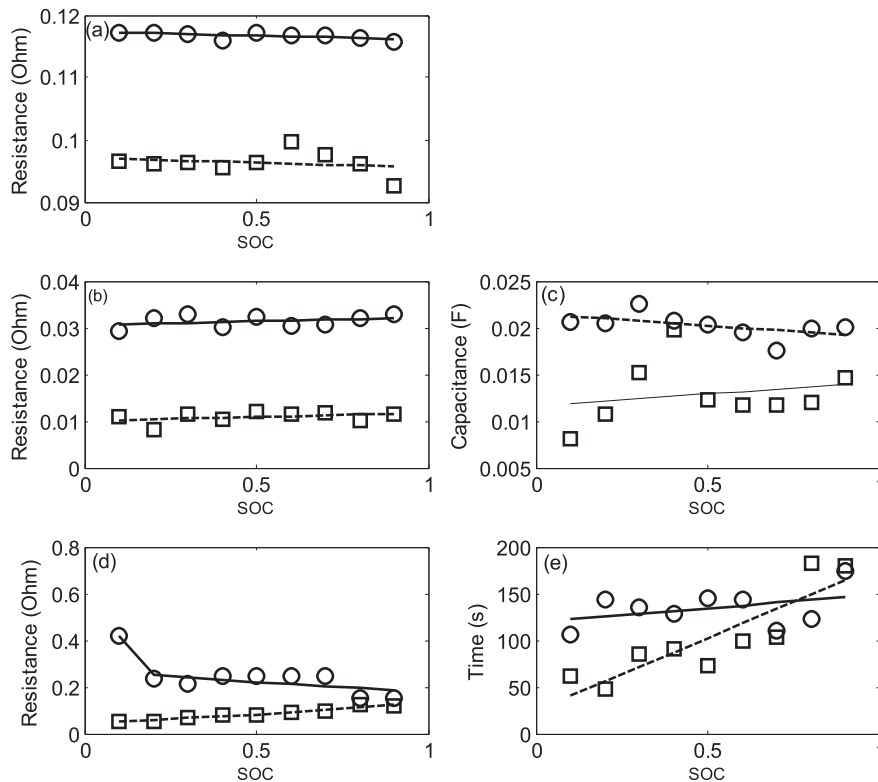


Fig. 3. Fitting equations for LFP (solid line) and LCO (dashed line) equivalent circuit parameters. Note that squares represent the measured LCO parameters and circles represent the measured LFP parameter where graph (a) is the element R_s , (b) R_{ct} , (c) C_{dl} , (d) R_W and (e) T_W .

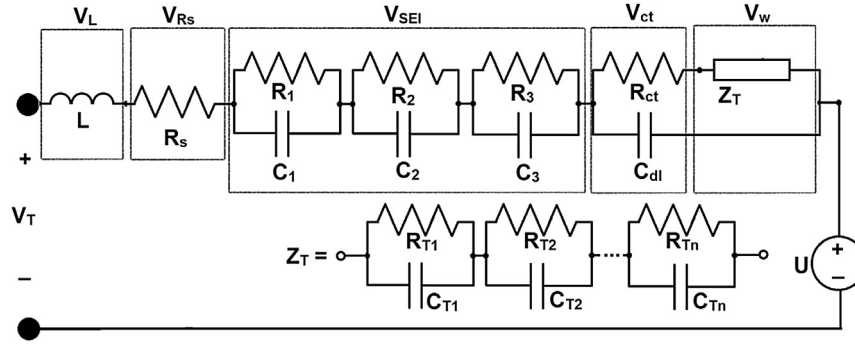


Fig. 4. Time-domain transform of the frequency-domain model of Fig. 2. Note that U is the open circuit potential of the cell at rest.

$$V_{SEI}(SOC) = \sum_{n=1}^3 I \times R_n(SOC) \times \left(1 - \exp\left(\frac{-t}{R_n(SOC) \times C_n(SOC)}\right) \right) \quad (3)$$

$$V_{ct||dl}(SOC) = I \times R_{ct}(SOC) \times \left(1 - \exp\left(\frac{-t}{R_{ct}(SOC) \times C_{dl}(SOC)}\right) \right) \quad (4)$$

$$V_{cint}(SOC) = I \times R_s(SOC) \times \left(1 - \exp\left(\frac{-t}{R_s(SOC) \times C_{int}(SOC)}\right) \right) \quad (5)$$

$$V_{Warburg}(SOC) = \sum_{n=1}^{\infty} I \times R_{T_n}(SOC) \times \left(1 - \exp\left(\frac{-t}{R_{T_n}(SOC) \times C_{T_n}(SOC)}\right) \right) \quad (6)$$

where R_{T_n} and C_{T_n} are defined by:

$$k_1(SOC) = R_W(SOC) \quad (7)$$

$$k_2(SOC) = \sqrt{\frac{R_W(SOC)}{T_W(SOC)}} \quad (8)$$

$$C_{T_n}(SOC) = \frac{k_1(SOC)}{2k_2(SOC)^2} \quad (9)$$

$$R_{T_n}(SOC) = \frac{8k_1(SOC)}{(2n-1)^2\pi^2} \quad (10)$$

where R_{T_n} and C_{T_n} are elements of the transmission line model representation of the Warburg diffusion element as discussed by Levi and Aurbach [20,25] and Maracher and Karden [7]. The equivalent transmission line model for the Warburg diffusion element can be seen in the insert in Fig. 4.

Based upon this transformation the PECMs for the LCO and LFP batteries were simulated in MATLAB™ against experimental discharges carried out on each cell using an Arbin BT2000. Fig. 5a and b shows the experimental and simulated discharge curves for each cell at various C-rates, while Fig. 6 depicts the effect of select voltage drops (Eqs. (2)–(10)) during a 1 C discharge simulation provide better understanding of the parameter effect as a function of terminal voltage.

4. Discussion

Under the paradigm that the PECM can approximate the parameters governing certain electrochemical processes in each cell well (with respect to the full cell), this discussion will attempt to ascribe equivalent circuit model parameters to phenomenological processes occurring in the cell and will show that these recorded parameter values are reasonable. The scope of this work will cover the charge transfer kinetics occurring in the Li-ion batteries (i.e. charge transfer resistance and electric double layer capacitance) and the ionic diffusion of Li-ions in the electrode(s). This discussion does not cover the intercalation capacitance, solid electrolyte interface (SEI) and the ohmic solution resistance of the cells that was calculated in the Modeling section of this paper. In the case of the former two, there was not an established methodology to validate our parameters against that is within our ability to test. In the latter case, the validation of the solution resistance was trivial in this case since the electrolyte, separator, and contacts were the same.

For the remaining circuit parameters the following observations could be made: The charge transfer resistance (R_{ct}) as defined as the speed of the surface reaction that facilitates the transference of ions across an electrode/electrolyte boundary [26] may also be represented by the exchange current density via:

$$i_0 = \frac{RT}{nFR'_{ct}} \quad (11)$$

where R represents the universal gas constant, T represents the temperature in Kelvin, n is the valence, F is Faraday's constant, and R'_{ct} is the charge transfer resistance per unit area.

Table 2 lists the charge transfer resistance and corresponding exchange current density of the LCO and LFP batteries as a function of SOC. The respective averages for the LCO and LFP battery exchange current densities are 8.75×10^{-3} and $2.7 \times 10^{-3} \text{ A cm}^{-2}$, respectively. From the data recorded, two conclusions may be made: First, the exchange current density of the full-cell LCO and LFP batteries is on the same order of magnitude as reported [25,27] half-cell (Li_xCoO_2 , Li_xFePO_4 , $\text{Li}_{1-x}\text{C}_6$) exchange current densities, leading to the conclusion that the model interpretation of the charge transfer resistance is accurate. Second, the general trend of marginally decreasing exchange current density during cell charging leads one to conclude that the exchange current densities are at least partially dominated by their cathode electrodes.

The first conclusion may be explained in greater detail: Values reported for Li_xCoO_2 by Garcia et al. [26] ranged from 2.5×10^{-3} to $3 \times 10^{-4} \text{ A cm}^{-2}$ underperformed compared to calculated results taken from EIS. This may be due to the difference between

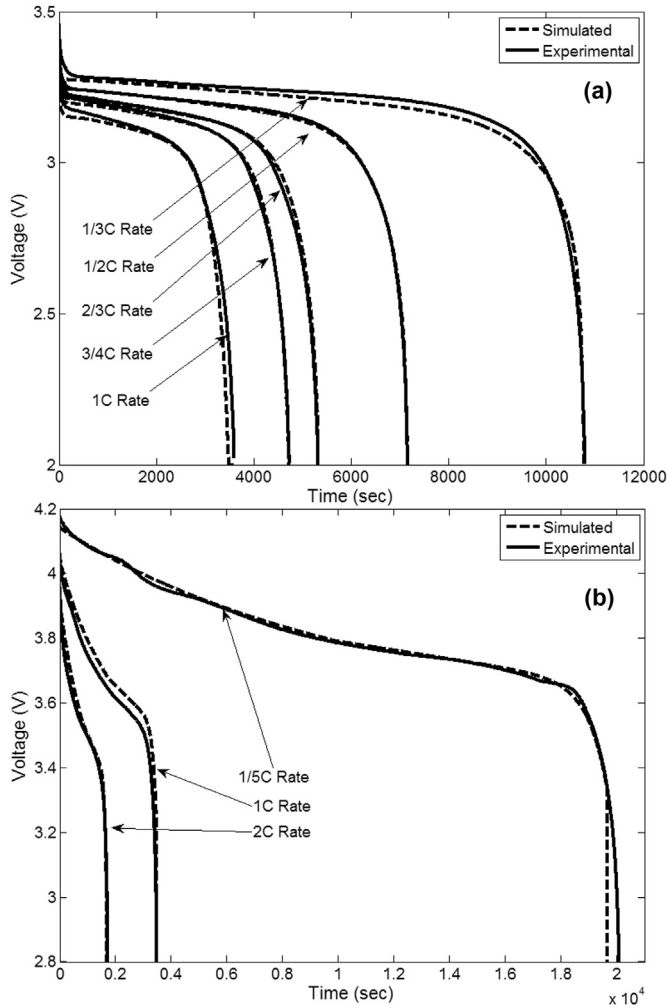


Fig. 5. Experimental and simulation results for (a) LFP cell at various C-rates and (b) LCO cell at various C-rates.

experimental and commercially manufactured cell construction, though the inherent error used in modeling R_{ct} via EIS may have also contributed to this discrepancy. In the case of the Li_xFePO_4 , the observed exchange current density of $2.7 \times 10^{-3} \text{ A cm}^{-2}$ is higher than reported by others [31,32] ($8 \times 10^{-5} \text{ A cm}^{-2}$) which may be explained again by the difference in producing cells in a laboratory vs. a commercial process.

The second conclusion may be explained further by relating the decreasing concentration of Li-ions at the cathode to a decrease in the magnitude of cathodic exchange current densities. This trend is well documented [26–31] when looking at half-cell performances. From this we may infer that the trends we observed are caused by the cathodic exchange current.

To model the electrochemical process of diffusion, the decision was made to use the Finite Length Warburg (FLW) element which models 1-D particle diffusion with a transmissive boundary condition. While the diffusion of Li-ions in LIBs is a vastly more complex system, especially in dealing with two-phase systems like Li_xFePO_4 and Li_xCoO_2 , previous work [5,6,34] has provided good agreement between EIS techniques and other methods (chiefly PITT) in determining diffusion aspects including the diffusion coefficient in LIBs.

In incorporating the FLW into our electric model, the Warburg coefficient (A_W) was determined via direct calculation (Eq. (12)) and

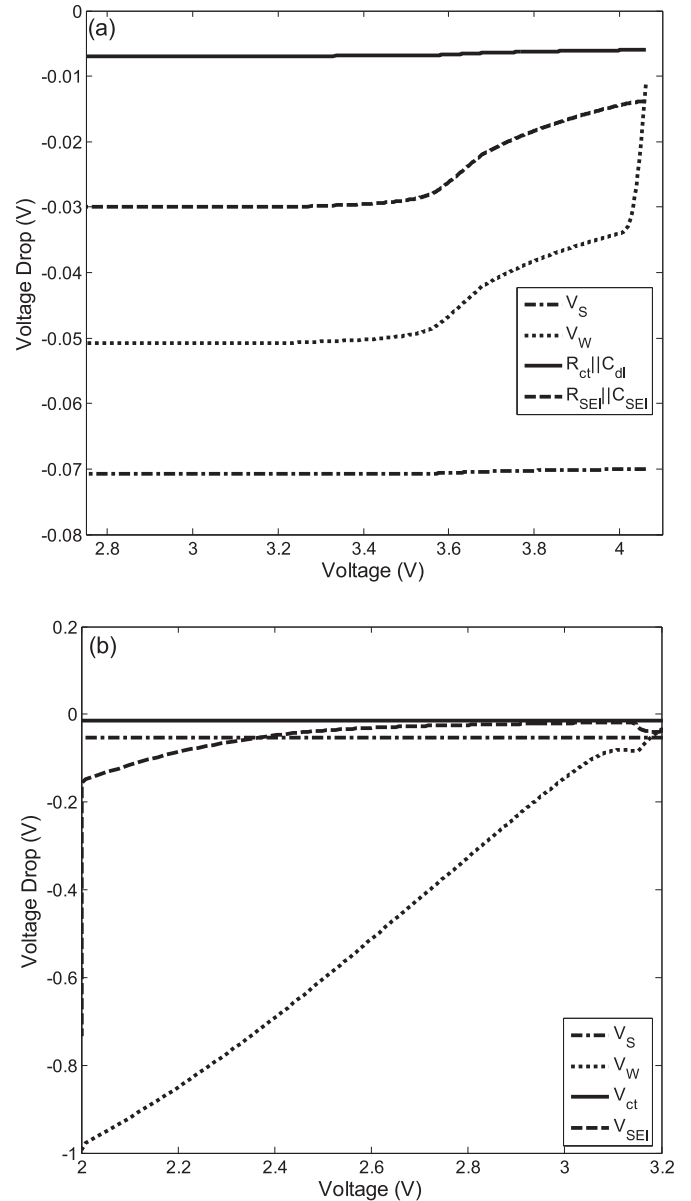


Fig. 6. Graphical representation of Eqs. (2)–(9) for (a) LCO full-cell and (b) LFP full cell for 1 C discharge as a function of terminal voltage.

validated via the graphical method by which the EIS diffusion tail is plotted $\text{Re}(Z)$ v. $1/(\omega)^{-1/2}$ or $\text{Im}(Z)$ v. $1/(\omega)^{-1/2}$ where the slope of the resulting lines is the Warburg coefficient. The difference between graphical and calculated Warburg coefficients are 7.45% and 11.46%

Table 2
Charge transfer resistance and exchange current density.

SOC	LFP R_{ct} (Ω)	LCO R_{ct} (Ω)	LFP i_0 (A cm^{-2})	LCO i_0 (A cm^{-2})
0.1	0.029196	0.010925	3.06×10^{-3}	9.01×10^{-3}
0.2	0.032104	0.00828	2.79×10^{-3}	1.19×10^{-2}
0.3	0.032888	0.011522	2.72×10^{-3}	8.54×10^{-3}
0.4	0.030225	0.010368	2.96×10^{-3}	9.49×10^{-3}
0.5	0.032384	0.012162	2.76×10^{-3}	8.09×10^{-3}
0.6	0.030461	0.01163	2.94×10^{-3}	8.46×10^{-3}
0.7	0.030568	0.011847	2.93×10^{-3}	8.31×10^{-3}
0.8	0.031983	0.010134	2.80×10^{-3}	9.71×10^{-3}
0.9	0.03282	0.011531	2.73×10^{-3}	8.54×10^{-3}

for the LCO and LFP, full cells respectively. This difference further shows good agreement between the PECM and EIS data.

$$A_W = \frac{RT}{n^2 F^2 S \sqrt{2D}} = \frac{R_W}{\sqrt{T_W}} \quad (12)$$

where X is the molar concentration of the species, S is the surface area of the electrode, D is the diffusion coefficient of the species, and R_W and T_W are the Warburg resistance and Warburg time constant respectively.

With the Warburg coefficient for the LCO and LFP full cells accurately determined, it may be possible to determine if one electrode dominates the diffusion coefficient of a full cell. Ye et al. [35] has shown that the Warburg resistance element (R_W) has an inversely proportional relationship to the diffusion coefficient (D_{Li}) in half cells. Also, numerous sources [36–41] report a relationship in which the diffusion coefficient in electrode materials are inversely proportional to the amount of lithium intercalated into the electrodes (i.e. D_{Li} decreases as x in Li_xFePO_4 , Li_xC_6 , or Li_xCoO_2 increases). In the case of the LCO cell (as seen in Table 3) the Warburg resistance increases with increasing SOC. From the relationships discussed above, if the Warburg resistance is increasing as Li-ions are being shuttled into the anode (ion concentration is increasing and diffusion coefficient is decreasing) then the EIS data presented is indicative of anode behavior. Similarly for the LFP full-cell, when seeing an increase in Warburg resistance with decreasing SOC it may be inferred that the EIS data is reflecting the cathode. Table 3 lists the calculated diffusion coefficient as a function of SOC, R_W as a function of SOC, and the calculated and graphically determined Warburg coefficients (A_W) as a function of SOC for the LCO and LFP cells.

$$D_{Li} = \frac{1}{2} \left(\frac{RT}{n^2 F^2 X S A_W} \right)^2 \quad (13)$$

Based upon this inference, the diffusion coefficient for each cell may be calculated as shown in Eq. (13). Based upon assumed molar concentrations and measured surface areas, the diffusion coefficient for the LFP cathode and LCO anode were 4.5×10^{-12} and $8.3 \times 10^{-11} \text{ cm}^2 \text{ s}^{-1}$, respectively. These diffusion coefficient values are within one order of magnitude as those reported by others [5,6,25,27,36,39,41–45] reinforcing the validity of the inference above.

With knowledge of the diffusion coefficient it may be possible to estimate the average particle size of the electrode in question (as postulated by Dell'Era and Pasquali [6]). Eq. (14) relates the effective particle radius (r) to the Nernst diffusion length (assuming spherical particle), δ , provided by Srinivasan and Wang [31].

$$\delta = \frac{r}{5} \quad (14)$$

where the Nernst diffusion length is related to the diffusion coefficient by the definition of the Warburg resistance (Eq. (14)).

$$R_W = \frac{RT\delta}{n^2 F^2 X S \sqrt{2D}} \quad (15)$$

From Eqs. (14) and (15), the average particle radii for the LFP cathode and LCO anode were calculated to be 1.2 and 4.6 μm , respectively. To see if these values were near real particle sizes for these cells, two commercial cells (one LFP and one LCO cell) were disassembled, their anodes and cathodes cleaned in EC solvent, dried, and then viewed under a scanning electron microscope (SEM). SEM results are presented in Fig. 7.

From Fig. 7 it can be seen that the average cathode particle radii for the LFP cell was approximately 0.5–1.0 μm while the average particle radii for the LCO anode was approximately 12 μm . In the case of the Li_xFePO_4 cathode, the calculated radius is almost double that of the SEM result while the calculated carbon anode radius was about one-third of the SEM result. This error may be due in large part to the orientation of the electrode materials as it is well documented that the orientation and shape of electrode particles [46,47] can dramatically affect the diffusion coefficient [34,37,48,49]. Also, in the case of the $LiFePO_4$ cathode, the model and method proposed do not account for any carbon painting on the $LiFePO_4$ particles, commonly performed to increase electronic conductivity [50]. As such, while it may still be possible to calculate the particle size accurately in some limited cases; in general the results discussed here do not support that claim.

The electric double layer capacitance (ELDC) observed is similar to those discussed [51–53] in which cathode and anode interfacial capacitances increase as their potential increases. In the case of a full cell, as the cell is charged, ions leave the cathode and intercalate into the graphitic anode matrix, corresponding to a potential decrease (V_{anode} v. Li-ion) at the anode and a potential increase ($V_{cathode}$ v. Li-ion) at the cathode. From the data provided in Table 4 the capacitance values designated to the EDLC remain fairly constant across the cells SOC.

Table 3
Warburg (diffusion) parameters.

Cell	SOC	R_W (Ω)	T_W (s)	A_W (graphical) ($\Omega \text{ s}^{-0.5}$)	A_W (calculated) ($\Omega \text{ s}^{-0.5}$)	D_{Li} ($\text{cm}^2 \text{ s}^{-1}$)	Average particle radius (μm)
LCO	0.1	0.055346	62.1	0.00700	0.00702	3.68×10^{-10}	4.60
	0.2	0.050749	47.5	0.00810	0.00735	1.57×10^{-10}	
	0.3	0.069428	85.0	0.00745	0.00753	8.69×10^{-11}	
	0.4	0.07909	91.5	0.00740	0.00826	4.69×10^{-11}	
	0.5	0.08157	72.9	0.00930	0.00937	2.57×10^{-11}	
	0.6	0.09168	100.0	0.00995	0.00900	2.06×10^{-11}	
	0.7	0.09900	103.9	0.00885	0.00971	1.36×10^{-11}	
	0.8	0.12317	182.4	0.00770	0.00912	1.23×10^{-11}	
	0.9	0.11849	179.4	0.00880	0.00884	1.06×10^{-11}	
LFP	0.1	0.42096	106.6	0.03205	0.04077	1.07×10^{-12}	1.20
	0.2	0.23455	143.1	0.02010	0.01960	2.95×10^{-12}	
	0.3	0.21352	135.9	0.01840	0.01831	3.83×10^{-12}	
	0.4	0.24803	127.8	0.02035	0.02194	3.41×10^{-12}	
	0.5	0.24818	145.7	0.02045	0.02056	3.7×10^{-12}	
	0.6	0.24692	144.0	0.01945	0.02057	4.49×10^{-12}	
	0.7	0.24702	110.0	0.02145	0.02355	4.08×10^{-12}	
	0.8	0.15503	122.7	0.01615	0.01399	7.98×10^{-12}	
	0.9	0.15229	175.0	0.01790	0.01151	7.25×10^{-12}	

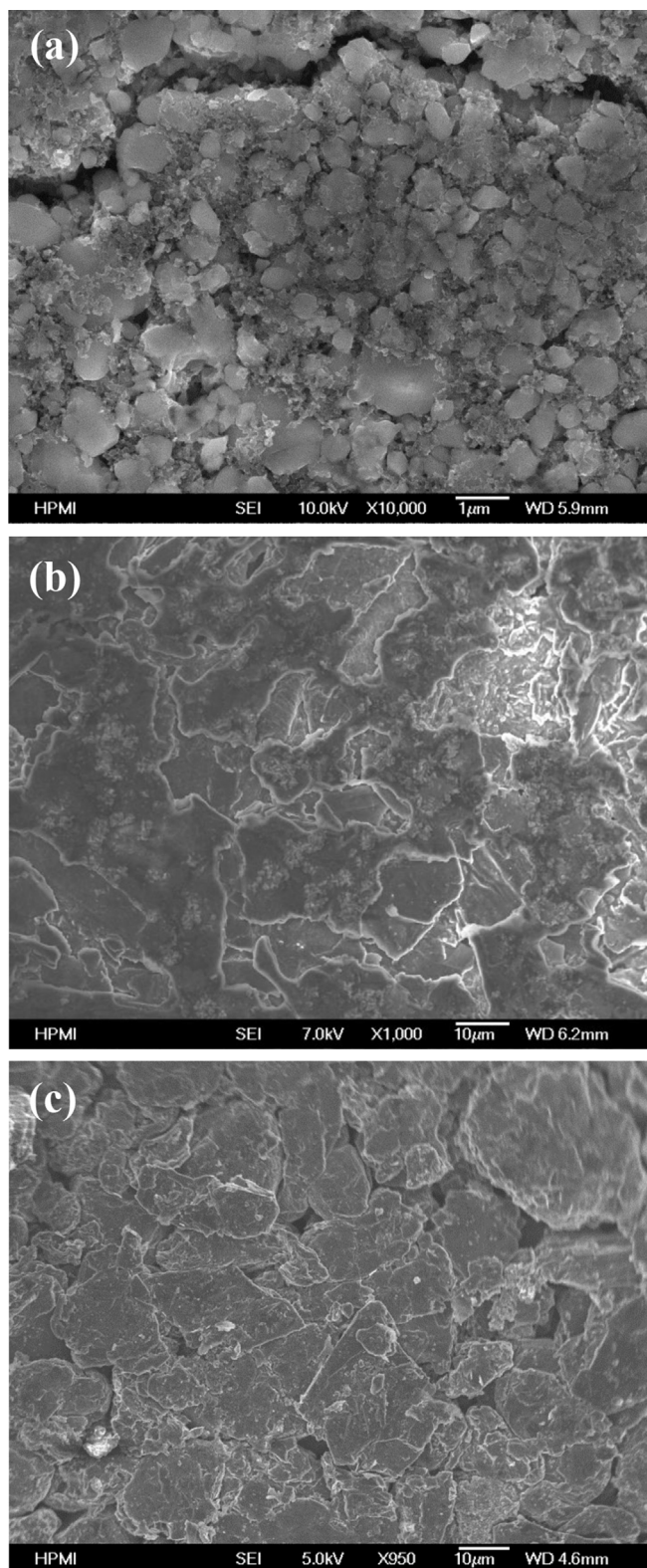


Fig. 7. SEM imaging of (a) Li_xFePO_4 -cathode at $\times 10,000$, (b) $\text{Li}_{1-x}\text{C}_6$ -anode at $\times 1000$ and (c) Cross section of same anode to see underneath presumed SEI layer at $\times 950$.

To validate the resulting measured EDLC, the surface area of the electrodes must be considered. The surface area was estimated based upon the average particle size described through SEM analysis, and the measured weights of electrode materials. Through algebraic manipulation of the assumed spherical particle surface

Table 4

Double layer capacitance as a function of SOC and surface area.

Cell	SOC	C_{dl} (F)	Calculated anode specific area ($\text{cm}_2 \text{g}^{-1}$)	Anode capacitance ($\mu\text{F cm}^{-2}$)	Avg. capacitance ($\mu\text{F cm}^{-2}$)
LCO	0.1	0.0206	237.45	28.99	28.47
	0.2	0.0205		28.88	
	0.3	0.0226		31.76	
	0.4	0.0208		29.23	
	0.5	0.0204		28.78	
	0.6	0.0195		27.41	
	0.7	0.0176		24.80	
	0.8	0.0200		28.11	
	0.9	0.0201		28.37	
LFP	0.1	0.0081	235.04	14.76	23.46
	0.2	0.0108		19.58	
	0.3	0.0152		27.64	
	0.4	0.0198		35.92	
	0.5	0.0123		22.32	
	0.6	0.0117		21.24	
	0.7	0.0118		21.32	
	0.8	0.0120		21.76	
	0.9	0.0147		26.66	

area and volume, along with the measured weight of the cathodes and anodes, the approximated surface area could be calculated. Table 4 reflects these surface areas. Since the surface areas between LFP and LCO cathodes and anodes vary by several orders of magnitude, the overall capacitance of the cell would be dominated by the smaller anodes. As a result, the capacitance values per unit area varied as a function of SOC from 0.292 to 0.274 F m^{-2} for the LCO anode, and 0.147–0.266 F m^{-2} . The approximate value for the EDLC for $\text{Li}_{1-x}\text{C}_6$ anodes is roughly 0.2 F m^{-2} has been reported [51–53]. By this comparison, it is reasonable to conclude that it is plausible based upon a rough calculation of surface area, that the anodes of both cells dominate EDLC as described by EIS and PECM.

5. Conclusion

By using a physical electric circuit model (PECM) that accurately models Li-ion battery performance, characterization of the electrochemical processes occurring inside two similar, commercial, Li-ion batteries was carried out. This novel method of applying phenomenological or physical-based equivalent circuit modeling to EIS data provided unique and non-destructive insight into the electrochemical processes inside two full-cell Li-ion batteries. Both cells were nearly identical with the exception of their cathodes (Li_xFePO_4 and Li_xCoO_2). From this analysis it was determined that the cathodes of both cells limited the exchange current densities, the Li_xFePO_4 cathode and $\text{Li}_{1-x}\text{C}_6$ anode of the LFP and LCO cells each limited the ionic diffusion, and the anodes of both cells were representative of the double layer capacitances described. It was shown that this technique provided this information which may be useful in determining the limitation of full-cell batteries without disassembly.

Acknowledgments

This work is supported by National Sciences Foundation (NSF) under Engineering Research Center Program No. EEC-0812121 and NSF Award No. 1001415.

References

- [1] K. Mizushima, P.C. Jones, P.J. Wiseman, J.B. Goodenough, *Mater. Res. Bull.* 15 (1980) 783–789.
- [2] A.K. Padhi, K.S. Nanjundaswamy, J.B. Goodenough, *J. Electrochem. Soc.* 144 (1997) 1188–1194.
- [3] H. Zhou, M. Einarsrud, F. Vullum-Bruer, *J. Power Sources* 238 (2013) 478–484.

- [4] M.J. Osiak, E. Armstrong, T. Kennedy, C.M. Sotomayor Torres, K.M. Ryan, C. O'Dwyer, *ACS Appl. Mater. Interfaces* 5 (2013) 8195–8202.
- [5] M.D. Levi, D. Aurbach, *Electrochim. Acta* 45 (1999) 167–185.
- [6] A. Dell'Era, M. Pasquali, *J. Solid State Electrochem.* 13 (2009) 849–859.
- [7] P. Mauracher, E. Karden, *J. Power Sources* 67 (1997) 69–84.
- [8] E. Karden, S. Buller, R.W. De Doncker, *Electrochim. Acta* 47 (2002) 2347–2356.
- [9] S. Buller, M. Thele, E. Karden, R.W. De Doncker, *J. Power Sources* 113 (2003) 422–430.
- [10] P.L. Moss, J.P. Zheng, G. Au, P.J. Cygan, E.J. Plichta, *J. Electrochem. Soc.* 154 (2007) A1020–A1025.
- [11] P.L. Moss, G. Au, E.J. Plichta, J.P. Zheng, *J. Electrochem. Soc.* 155 (2008) A986–A994.
- [12] P. Moss, Study of Capacity Fade of Lithium-ion Polymer Battery with Continuous Cycling & Power Performance Modeling of Energy Storage Devices (Dissertation), Florida State University, Tallahassee, FL, USA, 2008.
- [13] P.L. Moss, G. Au, E.J. Plichta, J.P. Zheng, *J. Electrochem. Soc.* 157 (2010) A1–A7.
- [14] M. Greenleaf, H. Li, J.P. Zheng, *IEEE Trans. Sustain. Energy* (2013) 1–6.
- [15] D.D. Macdonald, *Electrochim. Acta* 51 (2006) 1376–1388.
- [16] F. Ciucci, *Electrochim. Acta* 87 (2013) 532–545.
- [17] F. Ciucci, T. Carraro, W.C. Chueh, W. Lai, *Electrochim. Acta* 56 (2011) 5416–5434.
- [18] K.N. Allahar, D. Battocchi, G.P. Bierwagen, D.E. Tallman, *J. Electrochem. Soc.* 157 (2010) C95.
- [19] H. Blanke, O. Bohlen, S. Buller, R.W. De Doncker, B. Fricke, A. Hammouche, D. Linzen, M. Thele, D.U. Sauer, *J. Power Sources* 144 (2005) 418–425.
- [20] M.D. Levi, *J. Electrochem. Soc.* 146 (1999) 1279.
- [21] S. Rodrigues, N. Munichandraiah, A.K. Shukla, *J. Solid State Electrochem.* 3 (1999) 397–405.
- [22] M.D. Levi, Z. Lu, D. Aurbach, *Solid State Ionics* 143 (2001) 309–318.
- [23] V.S. Muralidharan, *Anti-Corros. Meth. Mater.* 44 (1997) 26.
- [24] H. Song, Y. Jung, K. Lee, L.H. Dao, *Electrochim. Acta* 44 (1999) 3513–3519.
- [25] M.D. Levi, D. Aurbach, *J. Phys. Chem. B* 101 (1997) 4630–4640.
- [26] B. Garcia, J. Farcy, J.P. Pereira-Ramos, N. Baffier, *J. Electrochem. Soc.* 144 (1997) 1179–1184.
- [27] G. Bajars, G. Kucinskis, J. Smits, J. Kleperis, A. Lusi, *IOP Conf. Ser. Mater. Sci. Eng.* 38 (2012) 012019.
- [28] T. Piao, S. Park, C. Doh, S. Moon, *J. Electrochem. Soc.* 146 (1999) 2794–2798.
- [29] K.M. Shaju, G.V. Subba Rao, B.V.R. Chowdari, *J. Electrochem. Soc.* 151 (2004) A1324–A1332.
- [30] Y.H. Rho, K. Kanamura, *J. Electrochem. Soc.* 151 (2004) A1406–A1411.
- [31] V. Srinivasan, C.Y. Wang, *J. Electrochem. Soc.* 150 (2003) A98–A106.
- [32] G.X. Wang, S. Bewlay, S.A. Needham, H.K. Liu, R.S. Liu, V.A. Drozd, J. Lee, J.M. Chen, *J. Electrochem. Soc.* 153 (2006) A25–A31.
- [34] M.S. Islam, D.J. Driscoll, C.A.J. Fisher, P.R. Slater, *Chem. Mater.* 17 (2005) 5085–5092.
- [35] S.H. Ye, J.Y. Lv, X.P. Gao, F. Wu, D.Y. Song, *Electrochim. Acta* 49 (2004) 1623–1628.
- [36] M. Safari, C. Delacourt, *J. Electrochem. Soc.* 158 (2011) A562.
- [37] P.J. Bouwman, B.A. Boukamp, H.J.M. Bouwmeester, P.H.L. Notten, *J. Electrochem. Soc.* 149 (2002) A699–A709.
- [38] A.V. Churikov, M.A. Volgin, K.I. Pridatko, A.V. Ivanishchev, N.A. Gridina, A.L. L'vov, *Russ. J. Electrochem.* 39 (2003) 531–541.
- [39] A.V. Churikov, A.V. Ivanishchev, I.A. Ivanishcheva, V.O. Sycheva, N.R. Khasanova, E.V. Antipov, *Electrochim. Acta* 55 (2010) 2939–2950.
- [40] K. Dokko, M. Mohamedi, Y. Fujita, T. Itoh, M. Nishizawa, M. Umeda, I. Uchida, *J. Electrochem. Soc.* 148 (2001) A422–A426.
- [41] A. Funabiki, M. Inaba, Z. Ogumi, S. Yuasa, J. Otsuji, A. Tasaka, *J. Electrochem. Soc.* 145 (1998) 172–178.
- [42] M. Doyle, J. Newman, A.S. Gozdz, C.N. Schmutz, J. Tarascon, *J. Electrochem. Soc.* 143 (1996) 1890–1903.
- [43] S.J. Harris, A. Timmons, D.R. Baker, C. Monroe, *Chem. Phys. Lett.* 485 (2010) 265–274.
- [44] Y. NuLi, J. Yang, Z. Jiang, *J. Phys. Chem. Solids* 67 (2006) 882–886.
- [45] K. Persson, V.A. Sethuraman, L.J. Hardwick, Y. Hinuma, Y.S. Meng, A. van der Ven, V. Srinivasan, R. Kostecki, G. Ceder, *J. Phys. Chem. Lett.* 1 (2010) 1176–1180.
- [46] A. Gupta, J.H. Seo, X. Zhang, W. Du, A.M. Sastry, W. Shyy, *J. Electrochem. Soc.* 158 (2011) A487–A497.
- [47] X. Zhang, W. Shyy, A. Marie Sastry, *J. Electrochem. Soc.* 154 (2007) A910–A916.
- [48] J. Xie, N. Imanishi, T. Matsumura, A. Hirano, Y. Takeda, O. Yamamoto, *Solid State Ionics* 179 (2008) 362–370.
- [49] P.J. Bouwman, Lithium Intercalation in Preferentially Oriented Submicron LiCoO₂ Films (Thesis), University of Twente, Enschede, Netherlands, 2002.
- [50] K. Striebel, J. Shim, V. Srinivasan, J. Newman, *J. Electrochem. Soc.* 152 (2005) A664–A670.
- [51] G. Sikha, R.E. White, B.N. Popov, *J. Electrochem. Soc.* 152 (2005) A1682–A1693.
- [52] I.J. Ong, J. Newman, *J. Electrochem. Soc.* 146 (1999) 4360–4365.
- [53] H. Gerischer, R. McIntyre, D. Scherson, W. Storck, *J. Phys. Chem.* 91 (1987) 1930–1935.